Flat Spin of Slender Bodies at High Angles of Attack

Hirotoshi Kubota,* Isao Arai,† and Masayoshi Matsuzaka†
University of Tokyo, Tokyo, Japan

Low-speed wind tunnel investigations are performed for the flat spin of slender bodies at high angles of attack at Reynolds numbers of $(1.2\text{-}4.4)\times 10^5$. Effects of the geometrical configuration of the model, freestream Reynolds number, and angle of attack on the flat spin motion are analyzed using spin rate measurements, in situ surface pressure distribution, and static aerodynamic characteristics. It is verified that the flat spin is caused by differences in flow patterns at the critical Reynolds number. The measured side moment can be used to predict the actual flat spin rate. The flat spin can be alleviated by causing early transition of the boundary layer with artificial surface roughness.

Nomenclature

C_N = normal force coefficient = normal force/$q_\infty S_{\text{ref}}$
C_n = flat spin moment coefficient = flat spin moment/$q_\infty S_{\text{ref}} L$
$C_n(0)$ = side (yawing) moment coefficient in absence of flat spin
C_p = pressure coefficient = $(p-p_\infty)/q_\infty$
C_Y = side force coefficent = side force/$q_\infty S_{\text{ref}}$
D = model base diameter
d = surface roughness height normalized by model base diameter
L = model length
L_1 = distance between nose and center of gravity
L_2 = distance between base and center of gravity
ℓ = nose cone length of model A
N = flat spin rate, rpm
n = number of tripping wires
p = pressure
p_∞ = freestream static pressure
q_∞ = freestream dynamic pressure
Re_∞ = freestream Reynolds number referred to model base diameter
Re_c = critical Reynolds number
Re_n = cross-flow Reynolds number = $Re_\infty \sin\alpha$
S_{ref} = reference area = $\pi D^2/4$
U_∞ = freestream velocity
$\bar{X}_G$ = center of gravity
X_G = nondimensional center of gravity = $\bar{X}_G/L$
α = angle of attack
θ = nose cone angle of model A
ϕ = circumferential coordinate
ψ = azimuthal angle for attachment of tripping wire
Ω = angular velocity, rps

Introduction

SPACE material processing by use of a sounding rocket is one of the more important space activities. For the recovery of the processed material, the payload is contained within the nose-cylinder separated from the rocket main body. The configuration of the nose-cylinder is a slender body with a blunted/sharp nose cone and a cylinder; the effective braking is attained by the ballistic deceleration at high angle of attack.

At the free-flight drop test of a prototype slender body a coupling of two motions was observed,[1] namely, rotation around the center of gravity (c.g.) of the model in the plane of the attack angle and translation of the c.g. The former motion tends to rotation at 90-deg incidence (rotation in the horizontal plane).[1] This motion is often called a "flat spin." A large rate of flat spin is undesirable because of stresses on the payload due to severe centrifugal force. It is expected that this flat spin is caused by aerodynamic effects, namely, the yawing moment by asymmetric side forces centered at a location different from the c.g.

A large number of studies concerning the viscous cross flow around slender bodies at high angle of attack have been performed since Allen and Perkins[2] presented the semiempircal correlation for normal force coefficient. Chapman and Keener,[3] Lamont and Hunt,[4] Clarkson et al.[5] and other authors have studied the characteristics of the side force acting on various types of slender bodies. The review papers by Ericsson and Reding[6,7] suggest that the high level of asymmetric side force strongly depends on the freestream Reynolds number and angle of attack.

Bearman,[8] and independently Kamiya et al.,[9] predicted the occurrence of such an asymmetric side force, on the basis of experimental results for two-dimensional circular cylinders, due to the fixation of a short bubble of separation on one side of the cylinder at the critical Reynolds number.

Although there are many experimental and analytical studies for static side forces or active spin around the axis of a slender body, there has been little systematic test simulation of the flat spin motion, to our knowledge, except for the low-speed wind tunnel experiments of coning motion by Yoshinaga et al.[10] The objectives of the present paper are to simulate the steady-state flat spin in the low-speed wind tunnel, and to correlate the measured spin with measured aerodynamic forces and moments. The meaning of the term "flat spin" is extended to rotation with high angle of attack, but mainly at 90 deg. The influence of the various parameters such as model dimensions, freestream Reynolds number, angle of attack, etc., is investigated, where special attention is given to the spin behavior in the region of the critical Reynolds number. An approximate analysis is formulated to predict the steady-state flat spin rate for several cases.

The suggestion by Yoshinaga et al.[11,12] is verified that, for the case of a cone-cylinder, the aysmmetric side force and the flat spin motion remain (this flat spin is referred to here as the "residual flat spin") even beyond the critical freestream

Presented as Paper 82-0054 at the AIAA 20th Aerospace Sciences Meeting, Orlando, Fla., Jan. 11-14, 1982; submitted Jan. 22, 1982; revision received Oct. 7, 1982.

*Associate Professor, Department of Aeronautics, Faculty of Engineering. Member AIAA.
†Research Assistant, Department of Aeronautics, Faculty of Engineering.

velocity for the cylinder because the tapered nose section with its decreasing local diameter successively reaches the critical condition at higher velocities. Further, a method of alleviating the flat spin is tested based on the idea that the difference of the flow separation patterns on the two sides of the body causes the asymmetric side force.

Description of the Wind Tunnel Experiment

Wind Tunnel and Models

The 1.5-m Göttingen-type low-speed wind tunnel at the Department of Aeronautics, Faculty of Engineering, University of Tokyo was used. The freestream velocity is approximately 9-30 m/s. Two kinds of model were used: a blunted cone-cylinder (model A) and the corresponding circular cylinder (model B), as sketched in Fig. 1. The model dimensions are tabulated in the figure. Except for the surface pressure measurement model, they are made of poly-vinyl-chloride (PVC) for the sake of weight reduction, with Duralmin for the supporting part (hatched region in the figure).

The freestream Reynolds number referred to the base diameter is $(1.2\text{-}4.4)\times 10^5$, which covers the critical Reynolds number for the circular cylinder, about $(3.4\text{-}3.6)\times 10^5$.

Test Procedures

Static Test (in the Absence of Flat Spin)

The static test (in the absence of flat spin) comprises the following procedures: 1) measurement of side force and side moment by the force balance, 2) measurement of surface pressure, and 3) flow visualization with the use of oil flow technique.

Dynamic Test (in the Presence of Flat Spin)

The model is supported at its center of gravity by the supporting rod which can freely rotate, so that the model has 1 degree of freedom of rotation. The rotational friction of the rod is small enough to be negligible. The overall supporting device is located leeward so as not to disturb the flow (Fig. 2).

1) The free rotation (flat spin) rate at a fixed angle of attack is measured by a tachometer with a photomultiplier, and recorded on 16-mm film.

2) The surface pressure distributions are measured during the steady flat spin motion. The pressure distributions at two axial locations on the model surface, viz., one on the cylindrical part (620 mm from the nose) and the other on the conical part (250 mm from the nose) for model A, can be measured. The number of the pressure taps are 46 on each row. The pressure transducer and scanner are located inside the model and rotate together with the model. The measured pressure signals are successively transferred via the slip ring to the data processing system after analog/digital conversion.

3) The flat spin motion is alleviated by the attachment of a tripping wire, or sand paper to give artificial surface roughness, in order to prevent asymmetric flow separation.

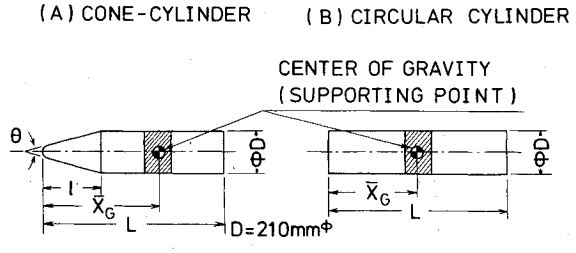

	MODEL	L, mm	θ, deg	l, mm	$\bar{X}_G$, mm	$X_G(=\bar{X}_G/L)$	ANGLE OF ATTACK α, deg
A	L80θ30	800	30	305	550	0.69	90, 75, 60, 45
		800	30	305	500	0.63	90
		800	30	305	450	0.56	90
		800	30	305	400	0.50	90
	L70θ30	700	30	305	500	0.71	90, 75, 60, 45
	L60θ30	600	30	305	450	0.75	90, 75, 60, 45
	L50θ30	500	30	305	400	0.80	90, 75, 60, 45
	L80θ20	800	20	452	615	0.77	90, 75, 60, 45
	L70θ20	700	20	452	565	0.81	90, 75, 60, 45
	L65θ20	650	20	452	515	0.79	90, 75, 60, 45
B	L80CYLINDER	800	--	---	400	0.50	90
	L70CYLINDER	700	--	---	350	0.50	90
	L60CYLINDER	600	--	---	300	0.50	90
	L50CYLINDER	500	--	---	250	0.50	90

Fig. 1 Models and dimensions.

Experimental Results on the Flow Characteristics and Flat Spin Simulation

Static Test

Side Force Coefficient C_Y

The effect of geometrical configuration of the models on the side force coefficient is shown in Fig. 3. The peak of the C_Y curve, which has been very steep for the two-dimensional circular cylinder at the critical Reynolds number region, $Re_c = (3.4\text{-}3.6)\times 10^5$ (Ref. 9), is slightly blunted for the three-dimensional slender body in this experiment. Decrease of the cone angle θ increases the three-dimensionality of the model and decreases the peak value of C_Y. The side force coefficient at the critical Reynolds number is approximately the same order of magnitude as the normal force coefficient.

The occurrence of the asymmetric side force corresponds to a difference in flow separation pattern as mentioned previously, and at the supercritical region, it is approximately zero for model B, while a residual side force at the nose cone exists for model A.

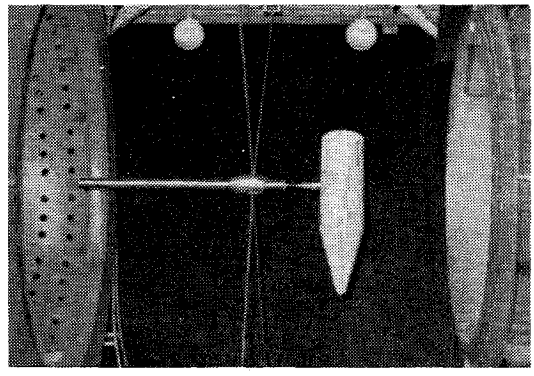

Fig. 2 Model supporting system.

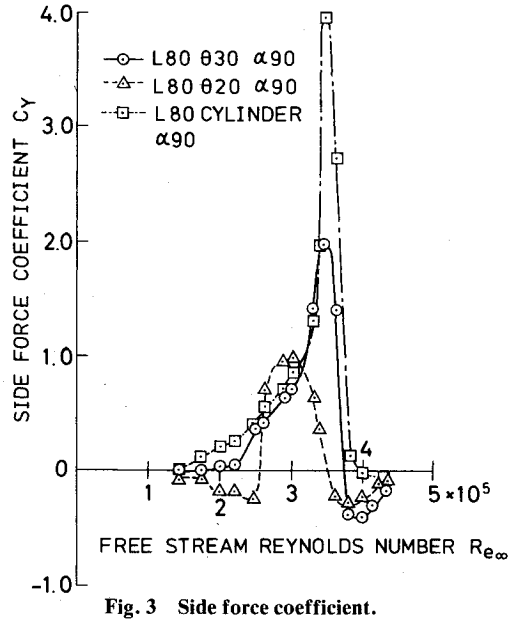

Fig. 3 Side force coefficient.

Side Moment Coefficient C_n (0)

The associated side moment coefficient is shown in Fig. 4 for the case of $L80\theta30\alpha90$ for three positions of the body c.g. The forward position of the c.g. causes the higher side moment because the center of pressure is located rather aft on this model. A significant increase in side moment can be seen in the critical Reynolds number region. The side moment for model B is small in the subcritical region.

Surface Pressure Coefficient C_p

Figure 5 shows the typical surface pressure distributions on the cylindrical part. In the subcritical region, the symmetric surface pressure distribution shows a well known laminar separation pattern, while, for higher Reynolds number near the critical region, locally different pressure levels seem to show indications of a subcritical bifurcation. A clear asymmetric pressure signature is seen when $Re_\infty = 3.25 \times 10^5$. Although this Reynolds number is considered a little lower than Re_c, the actual origin of the asymmetric side force may begin in this flow regime. The side force coefficient calculated from this pressure distribution agrees with the result of force measurements. Such asymmetries disappear in the supercritical region, and the pressure distribution then shows the typical turbulent separation pattern.

Provided that the local Reynolds number is based on the local diameter of the model, the Reynolds number for the conical part should be variable according to its decreasing local diameter.[11] Thus the surface pressure distributions on the cylindrical and conical parts are different from one another even for the same freestream velocity, because the local Reynolds number is different. The surface pressure asymmetries on the conical part are smaller than those on the cylindrical part.

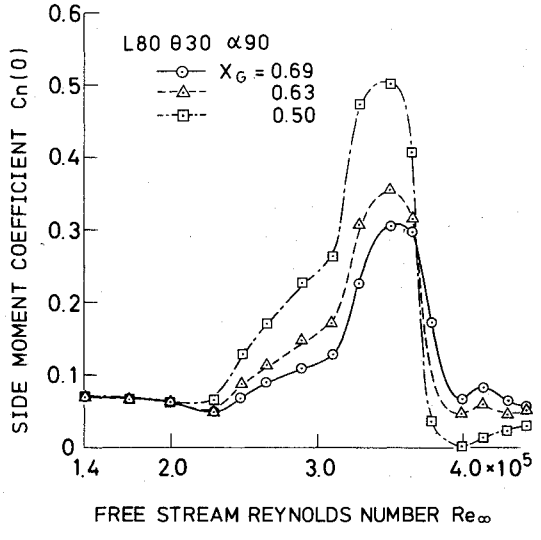

Fig. 4 Side moment coefficient in the absence of flat spin for model A.

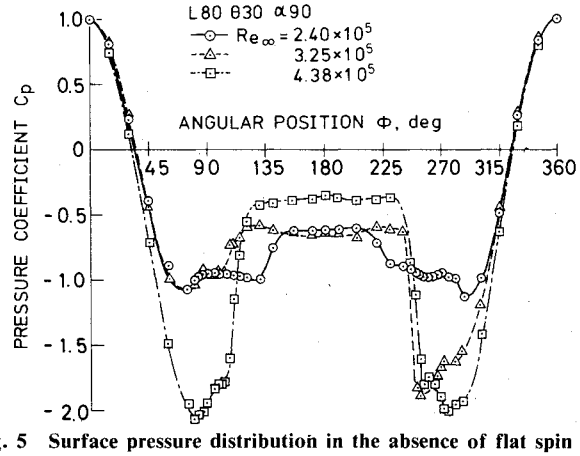

Fig. 5 Surface pressure distribution in the absence of flat spin for model A.

Flow Visualization

Figure 6 shows the simultaneous surface oil flow patterns on both sides of the model for three different freestream Reynolds numbers. The flow direction is illustrated in the photographs. The attached and the separated flow regimes appear black and white, respectively.

At $Re_\infty = 2.80 \times 10^5$ (subcritical both for the cylindrical and the conical parts), laminar separation is seen on both sides (separation angle is approximately 83 deg). At $Re_\infty = 3.53 \times 10^5$ (critical for the cylindrical part), the boundary layer on one side shows laminar separation, while the other side has the line of a short bubble on the cylindrical part. Beyond this flow region the asymmetric bubble line gradually diminishes and, for example, at $Re_\infty = 4.16 \times 10^5$, turbulent separation occurs on both sides with a separation angle of approximately 103 deg. Above $Re_\infty = 3.53 \times 10^5$, the oil flow patterns on the conical part suggest the origin of a residual side force.

Dynamic Test

Flat Spin Simulation

Figures 7a and 7b show the variations of flat spin rate with freestream and cross-flow Reynolds numbers. From a consideration of the nature of flow separation, it is clear that the probability of occurrence of the asymmetric side force in one direction is one-half[9]; hence the sign of N is unified in one direction for convenience in discussion.

A hysteresis of the side force appears when the Reynolds number increases and decreases[9]; this hysteresis is also observed in the flat spin rate (Fig. 7a). This also includes the contribution of the higher/lower circumferential velocity for the model. Data repeatability is fairly good.

The effect of the geometrical configuration of the model on the flat spin rate is also shown in Fig. 7a. For the model A, the flat spin rate increases at $Re_\infty \simeq Re_c$, which verifies the hypothesis that the asymmetric side force is caused by the difference of flow separation patterns in the region of critical Reynolds number. Also, the conical part is expected to reach the critical condition at successively higher velocities; therefore the spin rate does not decrease even though the freestream Reynolds number exceeds Re_c. The residual flat spin is rather high for the model of the smaller cone angle whose three-dimensionality is predominant. For model B, where the tip is located far from the supporting point, the circumferential velocity becomes large once the rotation begins, and the resultant velocity at the tip reaches the critical value at a relatively early stage. Accordingly, the flat spin rate rapidly increases at the subcritical freestream Reynolds number region. This remarkable behavior is seen in the case of the longer cylinder. A rapid decrease in the flat spin rate at Re_c is expected due to the small/no residual side moment in the supercritical Reynolds number region.

The effect of the model length is closely related to the three-dimensionality of the flow on the model. For the shorter model, the three-dimensional flow results in an increase in flat spin rate in the lower Reynolds number region; and the larger conical/cylindrical length ratio makes the residual flat spin continue for a wide range of Reynolds number. A similar three-dimensional effect occurs on longer models with smaller cone angles.

The effect of the angle of attack on the flat spin rate is shown in Fig. 7b. In accord with the small value of the asymmetric side force at $\alpha = 60$ and 75 deg, the flat spin rate there is not so large. Hence the flat spin in the horizontal plane ($\alpha = 90$ deg) is most probable.

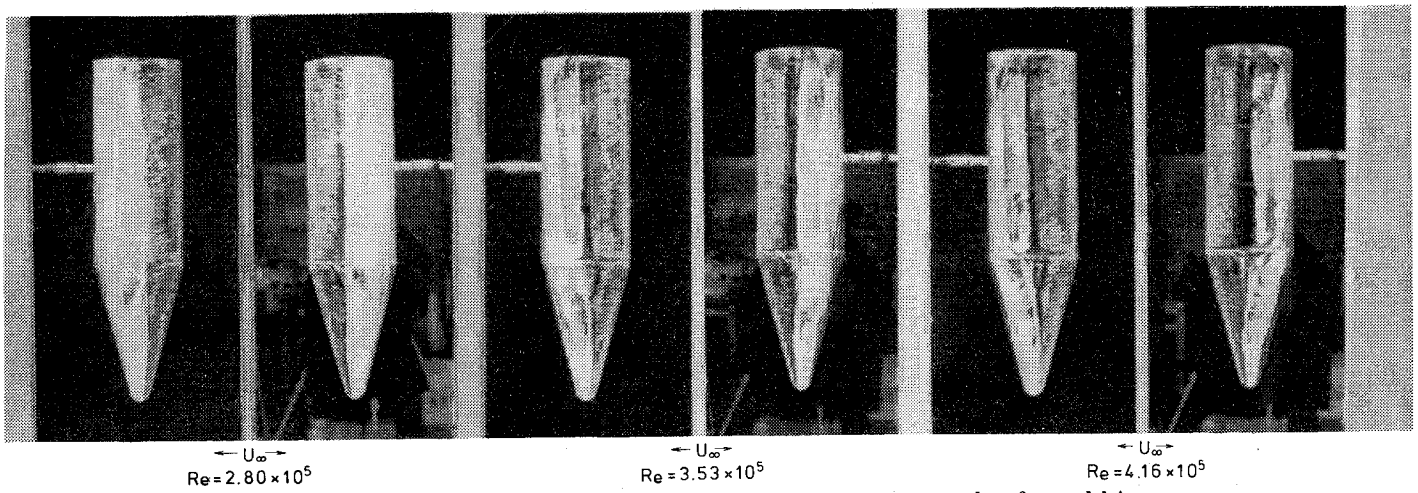

Fig. 6 Surface oil flow patterns for the representative Reynolds numbers for model A.

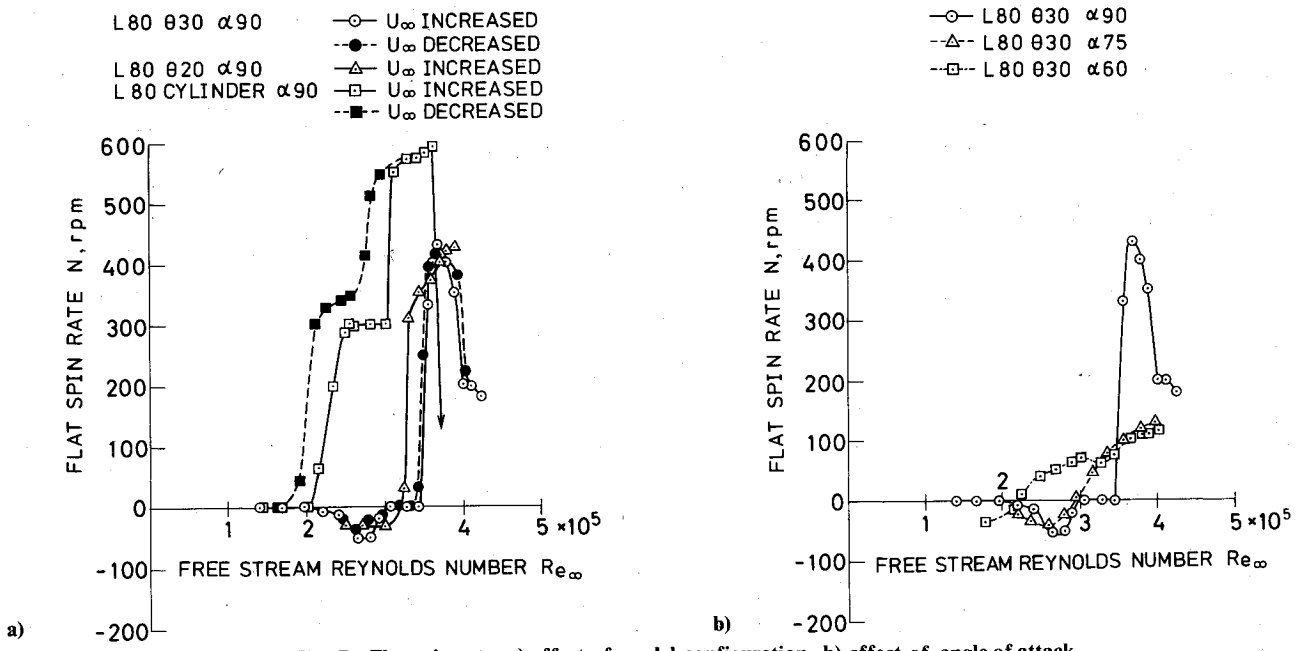

Fig. 7 Flat spin rate: a) effect of model configuration, b) effect of angle of attack.

The location of the c.g. has a significant influence upon the flat spin characteristics because the distance between the centers of pressure and gravity determines the side moment. The effect of the location of the c.g. on the flat spin rate will be discussed in a later section on analytical results.

Surface Pressure Distributions During Flat Spin Motion

Figure 8 shows a representative pressure distribution for model A. At the beginning of the rotation, the static pressure difference on both sides of the model causes the flat spin. Then, when the rotation reaches a steady state, the attained pressure distribution is due to the resultant flow induced by the rotation. The stagnation point for the resultant flow will vary with the rotation rate. The difference in the pressure levels between the sides, at $\phi = 90$ and 270 deg, becomes very large and the stagnation point deviation is about 27 deg. On the conical part it appears that the pressure difference is out of phase with that of the cylindrical part because of the rotation. For model B, the pressure distributions on the two cylindrical parts which are on opposite sides of the supporting point show a similar reversed phase pattern.

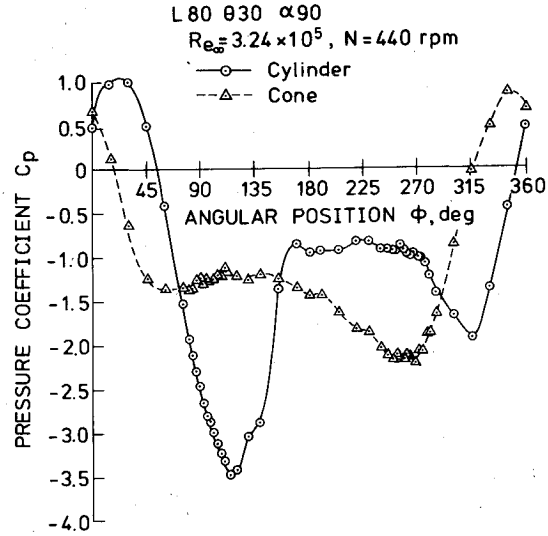

Fig. 8 Surface pressure distribution in the presence of flat spin for model A.

Approximate Analysis for Flat Spin Rate

The flat spin moment coefficient C_n should be written as

$$C_n = C_n(Re_\infty,\ X_G,\ \Omega) \tag{1}$$

With the assumption of continuous dependence of C_n on Ω, a Taylor-series expansion about $\Omega = 0$ will have the form

$$C_n = C_n(0) - \Omega[a(Re_\infty,\ X_G) - \Omega^2 b(Re_\infty,\ X_G)] \tag{2}$$

This is similar to the form of equation derived by Yoshinaga et al.[10]

At the steady state, $C_n = 0$. In Eq. (2), the terms $C_n(0)$, $\Omega a(Re_\infty,\ X_G)$, and $\Omega^3 b(Re_\infty,\ X_G)$ express the spin-driving moment, spin-damping moment, and spin-acceleration moment, respectively. For model A, the dominant terms are probably $C_n(0)$ and $a(Re_\infty,\ X_G)$, so that

$$N = 60\Omega \simeq 60C_n(0)/a(Re_\infty,\ X_G) \tag{3}$$

For model B, $C_n(0)$ is nearly zero by symmetry for $X_G = 0.5$, so that the steady-state flat spin rate will be reached when

$$N = 60\Omega \simeq 60\sqrt{a(Re_\infty,\ X_G)/b(Re_\infty,\ X_G)} \tag{4}$$

On the other hand, the coefficient for the spin-damping moment is reduced by using the normal force coefficient C_N according to the analysis of Ref. 13. Therefore $a(Re_\infty,\ X_G)$ can be expressed as

$$a(Re_\infty,\ X_G) = \frac{2\pi C_N}{U_\infty L^2}\,\frac{L_1^3 + L_2^3}{3} \tag{5}$$

Thus the predicted steady-state flat spin rate is calculated by Eqs. (3) and (5) using the measured normal force coefficient and side moment coefficient. The comparison between predicted and actual flat spin rates for two different locations of c.g. of model A is shown in Figs. 9a and 9b. In this calculation, the side moment coefficient of Fig. 4 was used.

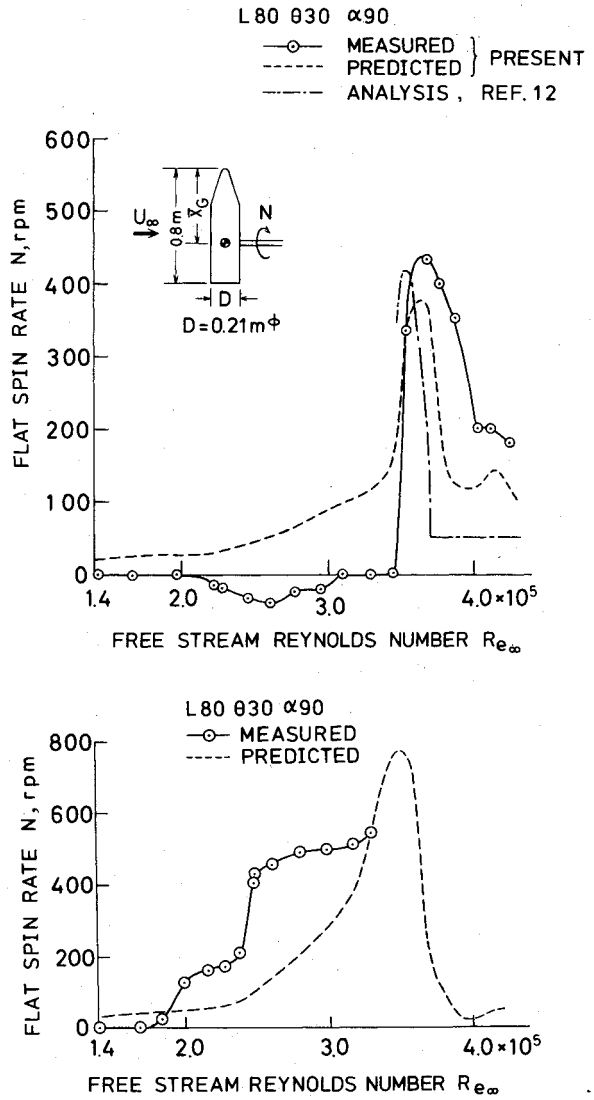

Fig. 9 Comparison of predicted flat spin rate with measured flat spin rate: a) $X_G = 0.69$, b) $X_G = 0.50$.

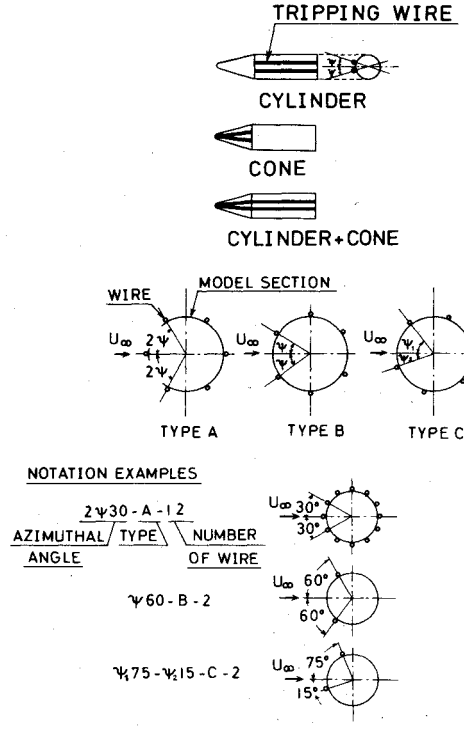

Fig. 10 Pattern of tripping wire attachment.

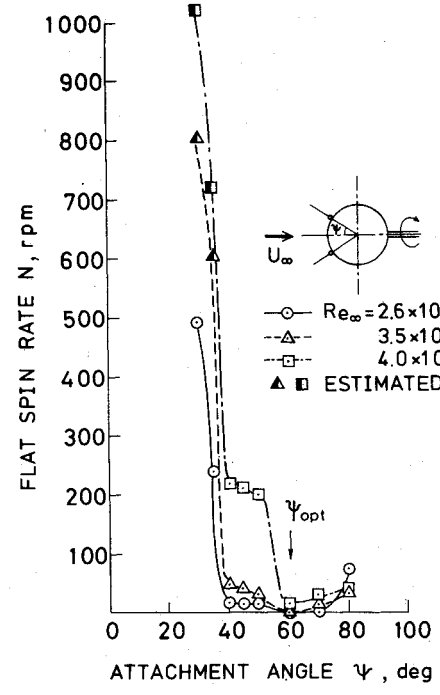

Fig. 11 Flat spin rate with the attachment of two tripping wires on only the cylindrical part of model A; $d = 0.007$.

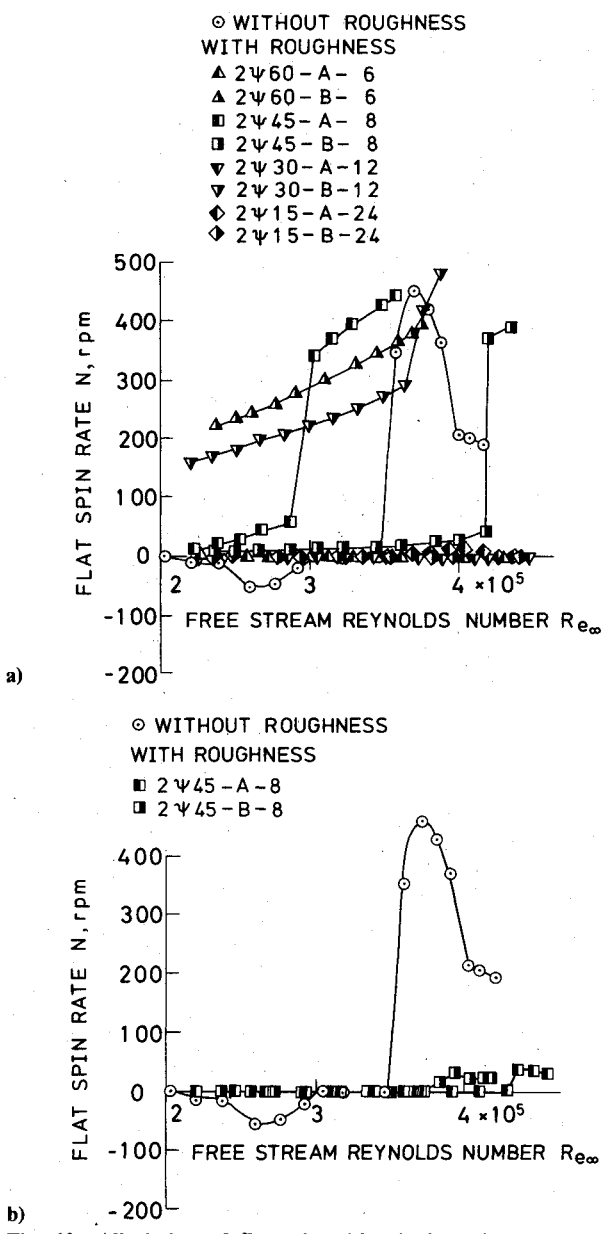

Fig. 12 Alleviation of flat spin with tripping wire on the whole periphery of a cross section of the cylindrical part of model A: a) $d=0.007$, b) $d=0.014$.

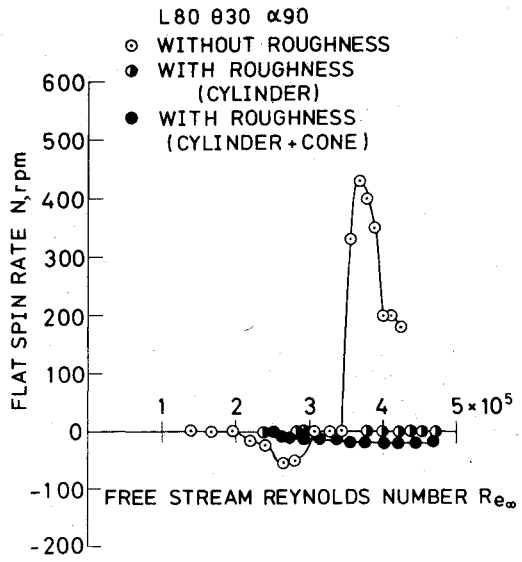

Fig. 13 Alleviation of flat spin with sand paper on the cylindrical part of model A.

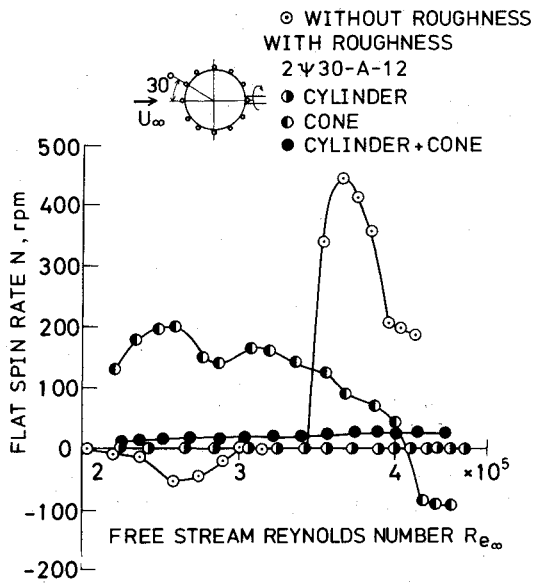

Fig. 14 Effect of mode for tripping wire attachment on flat spin rate; $d=0.007$.

Fairly good agreement is seen for the case of $X_G=0.69$, also with the analysis by Yoshinaga et al.,[11] while, for the case of $X_G=0.50$, the actual spin rate rises higher than the predicted one in the subcritical region. The reason is believed to be that the local resultant velocity of the freestream and circumferential velocities reaches the critical value and then the spin-driving moment abruptly increases. A similar tendency was seen for shorter models.

For model B, the actual flat spin rate unexpectedly increases in the subcritical region where the spin-driving moment must still be small. It is reasonable to consider that the nonlinear spin-acceleration moment $\Omega^3 b(Re_\infty, X_G)$ is important there, combined with the fact that local resultant velocity reaches the critical one.

In general, Eq. (2) seems to be an adequate representation for the analysis of the flat spin which can explain the experimental results.

Alleviation of Flat Spin

For practical applications, it is necessary to find a device to alleviate the above-mentioned flat spin motion. According to the concept that the flat spin is caused by aerodynamic forces, an effective way to alleviate spin would be to promote early transition of the boundary layer. This can be done by the use of artificial surface roughness. Both whole surface roughness[14] and a helical tripping wire[15] have been tested.

In the present investigation, a systematic flat spin alleviation is tried with the use of a straight tripping wire. For model A, tripping wires with normalized heights of 0.007, 0.010, and 0.014 were applied. In order to investigate the effect on the conical part, three modes for wire attachment as sketched in Fig. 10 were tested.

Tripping Wire Attachment Only on the Cylindrical Part

Figure 11 shows an example of the flat spin rate with the attachment of two tripping wires of type B (see the illustration in Fig. 10). The steady flat spin rate was obtained for the wire attachment at various azimuthal angles. It seems that an optimal angle exists for alleviation of flat spin; they are approximately 60, 50, and 40 deg for the nondimensional wire heights of 0.007, 0.010, and 0.014, respectively. For smaller angles, the flow tripped upstream again reattaches in the downstream region, so that the flow condition becomes similar to the case without tripping wire; therefore the side

force and thus the flat spin rate increases. For larger angles, the laminar separation occurs before it is tripped. This case is also similar to that without tripping wire. Thus a too small or large azimuthal angle for the attachment of the two tripping wires causes a large flat spin motion.

The fact that a too small attachment angle may produce a large flat spin rate is confirmed by the result of the side moment coefficient for the model ψ30-*B*-2 obtained by changing the location of the stagnation point.

For practical uses, it is necessary to find out the minimum number of tripping wires on the whole periphery required in order to prevent flat spin for any direction of the freestream. Figures 12a and 12b show the results in which the number of tripping wires is gradually increased for both types A and B. The minimum number of wires for flat spin alleviation of any type was 24 and 8 for the nondimensional heights of 0.007 and 0.014, respectively. This can be explained by the fact that high surface roughness has a greater tripping effect on the flow, hence a smaller number of wires is sufficient. The surface pressure distributions on the spin-alleviated model are exactly symmetric. The limiting case ($n \to \infty$) is attained by the attachment of sand paper. The result is shown in Fig. 13, which shows that the expected alleviation of flat spin occurs.

Our anticipation has been that the existence of the conical part without any spin-alleviation device causes the residual flat spin beyond Re_c even though the cylindrical part does not. However, as seen in Fig. 14, the spin rate is approximately zero, contrary to this expectation. This can be explained assuming that the asymmetric side force acting on the conical part appears intermittently. Thus, in some cases, the residual flat spin due to the existence of the conical part may be caused at higher Reynolds number than tested in the present experiment.[16]

Tripping Wire Attachment Only on the Conical Part

Figure 14 shows that the surface roughness on the conical part with a smaller diameter makes the critical Reynolds number lower, and this effect causes the large flat spin rate in the lower Reynolds number region, which is undesirable from a practical standpoint.

Tripping Wire Attachment Both on the Cylindrical and Conical Parts

In Fig. 14, it is seen that the flat spin rate is small, but larger than the case with wire attachment only on the cylindrical part. For the effective alleviation of the flat spin, it is enough to attach the artificial surface roughness only on the cylindrical part of the model.

Conclusions

The major conclusions are as follows:

1) The flat spin motion was able to be simulated for the three-dimensional slender bodies in the wind tunnel. The effect of the various parameters on the flat spin rate was investigated, in association with static force and side moment measurements, and surface pressure measurements made during the flat spin motion.

2) The difference of flow separation patterns on both sides of the model, which is considered to cause the asymmetric side force, was recognized by surface pressure distribution and flow visualization by an oil flow technique mainly at the flow region of the critical Reynolds number.

3) The approximate analysis can roughly explain the flat spin rate both for models A and B using the static side moment and normal force coefficients. Also the measured flat spin rate qualitatively agreed well with the analysis of Yoshinaga et al.

4) The flat spin was alleviated by causing early transition of the boundary layer with the use of artificial surface roughness. This is a very feasible method for preventing flat spin in practical use. The location, the minimum number, and the attachment azimuthal angle of straight tripping wires required to prevent flat spin were determined for each wire height.

Acknowledgments

The authors are greatly indebted to Prof. A. Takano for his valuable advice and suggestions. We would also like to express sincere thanks to M. Shirouzu, Dr. K. Soga, and Dr. I. Wada of the National Aerospace Laboratory for their initial encouragement of this research and for their useful comments. The present work was partly supported by a Grant-in-Aid for Scientific Research from the Ministry of Education of Japan.

References

[1] Shirouzu, M., Kubota, H., and Shibato, Y., "Aerodynamic Aspects on Recovery of Sounding Rocket Payload," Paper IAF-80-E-214 presented at the 31st Congress of International Astronautical Federation, Sept. 1980.

[2] Allen, H.J. and Perkins, E.W., "Characteristics of Flow Over Slender Inclined Bodies of Revolution," NASA RM A50L07, March 1951.

[3] Chapman, G.T. and Keener, E.R., "The Aerodynamics of Bodies of Revolution at Angle of Attack to 90°," AIAA Paper 79-0023, Jan. 1979.

[4] Lamont, P.J. and Hunt, B.L., "Pressure and Force Distributions on a Sharp-Nosed Circular Cylinder at Large Angles of Inclination to a Uniform Subsonic Stream," *Journal of Fluid Mechanics,* Vol. 76, Part 3, Aug. 1976, pp. 519-559.

[5] Clarkson, M.H., Malcolm, G.N., and Chapman, G.T., "A Subsonic, High Angle of Attack Flow Investigation at Several Reynolds Numbers," *AIAA Journal,* Vol. 16, Jan. 1978, pp. 53-60.

[6] Ericsson, L.E. and Reding, J.P., "Vortex-Induced Asymmetric Loads on Slender Vehicles," Final Technical Report, LMSC-D630807, Lockheed Missiles and Space Company Inc., Jan. 1979.

[7] Ericsson, L.E. and Reding, J.P., "Steady and Unsteady Vortex-Induced Asymmetric Loads on Slender Vehicles," *Journal of Spacecraft and Rockets,* Vol. 18, March-April 1981, pp. 97-109.

[8] Bearman, P.W., "On Vortex Shedding from a Circular Cylinder in the Critical Reynolds Number Regime," *Journal of Fluid Mechanics,* Vol. 37, Part 3, July 1969, pp. 577-585.

[9] Kamiya, N., Suzuki, S., and Nishi, T., "On the Aerodynamic Force Acting on a Circular Cylinder in the Critical Range of the Reynolds Number," AIAA Paper 79-1475, July 1979.

[10] Yoshinaga, T., Tate, A., and Inoue, K., "Coning Motion of Slender Bodies at High Angles of Attack in Low Speed Flow," AIAA Paper 81-1899, Aug. 1981.

[11] Yoshinaga, T., National Aerospace Laboratory, private communication, Feb. 1979.

[12] Yoshinaga, T., Tate, A., and Inoue, K., "Approximate Calculation of Aerodynamic Coefficients for Rotating Slender Bodies at 90 deg Incidence," *Journal of Spacecraft and Rockets,* Vol. 19, Jan.-Feb. 1982, pp. 84-86.

[13] Research Group for Recovery of Sounding Rocket Payloads, "Investigation on High-Angle-of-Attack Aerodynamic Characteristics of a Payload of a Sounding Rocket for Material Processing Experiments. III. On a Flat-Spin in Airdrop Test," NAL TM-426, National Aerospace Laboratory, Dec. 1980 (in Japanese).

[14] Pick, G.S., "Investigation of Side Forces on Ogive-Cylinder Bodies at High Angles of Attack in the M = 0.5 to 1.1 Range," AIAA Paper 71-570, June 1971.

[15] Rao, D.M., "Side Force Alleviation on Slender, Pointed Forebodies at High Angles of Attack," *Journal of Aircraft,* Vol. 16, Nov. 1979, pp. 763-768.

[16] Kamiya, N., Suzuki, S., Nakamura, M., and Yoshinaga, T., "Some Practical Aspects of the Burst of Laminar Separation Bubbles," Paper ICAS-80-10 presented at the 12th Congress of the International Council of the Aeronautical Sciences, Oct. 1980.